J. Appl. Cryst. (in press, 2005)

Quantitative Texture Analysis with the HIPPO TOF Diffractometer

S. Matthies, J. Pehl, H.-R. Wenk
Dept. Earth and Planetary Science, University of California at Berkeley, CA 94720

L. Lutterotti
Dip. Ingegneria dei Materiali e della Produzione Industriale, Università di Trento, Italy

S. C. Vogel
Los Alamos Neutron Science Center, Los Alamos, New Mexico 87545

Abstract

One of the design goals of the neutron time-of-flight (TOF) diffractometer HIPPO (HIgh Pressure - Preferred Orientation) at LANSCE (Los Alamos Neutron Science Center) was efficient quantitative texture analysis. In this paper, the effects of the HIPPO detector geometry and layout on texture analysis, particularly the shape and dimensions of the detector panels, are investigated in detail. An equal-channel angular-pressed (ECAP) aluminum-sample with a strong texture was used to determine the methodological limitations of various methods of quantitative texture analysis. Several algorithms for extracting the orientation distribution function (ODF) from the TOF-spectra are compared: discrete orientations at arbitrary positions, harmonic method in Rietveld codes (MAUD and GSAS) and discrete methods in MAUD. Because of the detector geometry, the sharpest texture peaks that can be represented are 12-15° in width, resulting in an optimal texture resolution of 25-30°. Due to the limited resolution and incomplete pole figure coverage, harmonic expansions beyond L = 12 introduce subsidiary oscillations, which are consistently identified as artifacts. Only discrete methods provide a quantitative representation of the texture. Harmonic methods are adequate for a qualitative description if the main texture component. The results of our analysis establish HIPPO as an efficient instrument to determine preferred orientations in relatively short measuring times.

Key words:
Neutron diffraction, Texture analysis, Harmonic method, WIMV, Rietveld, Aluminum

1. Introduction

The HIPPO diffractometer (for HIgh Pressure - Preferred Orientation, two of its main functions) at LANSCE (Los Alamos Neutron Science Center) became available to the LANSCE user program in summer 2002. Technical details and a first application to texture analysis have been given by Wenk *et al*. (2003). In this paper, we use experimental and analytical results to derive the characteristic parameters of the HIPPO spectrometer for quantitative texture analysis. We also summarize the unique features of this instrument and compare the procedures currently available for data analysis. The intent of this study is not to compare different texture measurement strategies for the same sample, but only to compare different analysis techniques for the same dataset.

An advantage of pulsed polychromatic neutrons and a detector system that can measure the time of flight (TOF) of neutrons and discriminate their energies is that whole spectra with many Bragg peaks can be recorded simultaneously and each Bragg reflection originates from differently oriented crystals. With TOF neutrons and a multi-detector system, fewer sample rotations are necessary to perform quantitative texture analysis. For typical texture investigations with HIPPO, rotation around a single axis is sufficient, which eliminates the need for a 2-circle goniometer and simplifies the construction of environmental cells to measure textures at non-ambient conditions. The reliability of neutron texture measurements was highlighted by excellent results of a round-robin experiment in which over 15 facilities participated (Wenk, 1991, Walther *et al*., 1995, Von Dreele, 1997) and, if it were more available, neutron diffraction would clearly be the method of choice for texture measurements of bulk samples. The round-robin experiment documented that pole figure measurements with neutron diffraction of the same sample by different laboratories are much more reproducible than those with conventional x-ray diffraction or electron microscopy. This is mainly because of the larger number of grains probed with neutrons, i.e. better grain statistics, negligible surface preparation effects, and the absence of instrument dependent defocusing and absorption corrections. We have shown earlier that HIPPO textures of the same round-robin sample are very similar to those measured at other facilities but with measuring time reduced to a few minutes compared to hours (Wenk *et al*., 2003).

In the present paper we will describe a more detailed analysis of the characteristic texture-related parameters of HIPPO, together with a comparison of different methods of quantitative data analysis, using a strongly textured ECAP aluminum sample.

2. Instrument characteristics

In designing a TOF neutron diffractometer, a compromise must be reached between intensity (decreasing approximately with $1/L^2$, where L is the flight path length between moderator and sample) and d-spacing resolution (increasing approximately with 1/L). The goal for HIPPO was to have the highest count rates available at the cost of only moderate d-spacing resolution, which was achieved by an instrument design consisting of detectors covering a large solid angle, and a short incident flight path of 9 m. HIPPO views a decoupled high intensity/low resolution water moderator of 2.5 cm thickness with a square surface of 13×13 cm^2. The time-averaged flux on a sample in HIPPO, with the proton accelerator operating at 120 μA and 20 Hz, is $\sim2.4\times10^7$ neutrons s^{-1} cm^{-2} for neutron energies in the "thermal" (<0.4 eV) range suitable for diffraction work (Ino *et al.*, 2004). Details about spallation neutron production at LANSCE are described by Roberts (1999).

1,360 ^{3}He detector tubes are arranged in 50 panels on five rings (banks) surrounding the incident beam (Figure 1). The detector layout comprises five angular ranges, covering both low and high diffraction angles and characteristics of each range are listed in Table 1. The d-spacings are determined from the chosen TOF range of 0.75 ms to 24 ms. The total detector coverage is 4.74 m^2. Detector tubes are not position sensitive along their length, which ranges from 46 cm for the backscattering angle to 15 cm for the most forward scattering angle.

The large sample chamber is built to accommodate a variety of ancillary equipment. It has an opening 81.28 cm (32 in) above the neutron beam centerline with a LANSCE-standard diameter of 71.12 cm (28 in), allowing interchange of ancillary equipment with other LANSCE beamlines. The walls of this chamber are 6.3 mm aluminum to minimize attenuation of scattered neutrons while maintaining structural stability. The 90° panels view the sample through 1.5 mm thick aluminum beam windows to optimize detection of diffracted intensity from high-pressure experiments. For most experiments the chamber is not evacuated during the course of an experiment, although evacuation is possible to reduce air scattering. A range of ancillary equipment is available to HIPPO users, including cryogenic equipment (displex system capable of 10 K to 300 K), high temperature vacuum furnaces (300 K to 1400 K) (Wenk *et al*. 2004), a toroidal-anvil high-pressure cell (20 GPa and 2000 K with 1 mm^3 sample volume), a gas-cell (10 kbar and 20K with 1 cm^3 sample volume) (Lokshin *et al.* 2004), a multi-position sample changer/goniometer, and a 100 kN uniaxial load frame (Vogel *et al*., 2004). The large sample chamber also allows users to design their own sample environments, as was used to analyze the crystal structure changes during charging and discharging a commercial Li-ion battery (Rodriguez *et al*., 2004). So far texture measurements have been performed with the multi-position sample changer, the displex system and the high-temperature vacuum furnace. The automated sample changer was used for the texture experiment described below. We used the $2\Theta = 140°$, 90° and 40° detector banks only, because of the poor d-spacing resolution of the 10° and 20° detectors.

The TOF data from the detector tubes are summed for each detector panel or, if orientation information is not important, into one histogram containing all detector panels of a bank. The required TOF-shift for each tube is obtained from a calibration with CaF_2 or silicon. Based on this calibration the raw data are binned into a compact ASCII file in GSAS format (Larson & Von Dreele, 1994) that is provided to the user for further analysis. Figure 2 displays all spectra recorded on one detector panel from each ring for the aluminum sample in 4 rotation positions. With decreasing diffraction angle, the resolution in d-spacing decreases, resulting in broader peaks. The diffracted intensity increases with decreasing diffraction angle and counting statistics improve. The results are broader peaks and a much smoother curve from the 40° detectors than from the 90° and 140° detectors. Within one bank relative intensities of a given diffraction peak vary with rotation. This is an indication of preferred orientation in the sample and the relative intensity differences are used to extract texture information as will be described in Section 4.

3. Pole figure coverage and detector geometry

Angular resolution *b* for texture information describes the minimum resolvable difference between texture components in the ODF space. Two peaks in orientation space of an instrument-dependent minimum width, separated by less than the angular resolution, will be seen as a single peak. In this section, we derive the geometrical angular resolution for texture analysis with HIPPO data. Because of the size and shape of a detector panel, each detector

records a range of crystal orientations. For a single sample orientation, the detector panels from the 140°, 90°, and 40° banks roughly cover one quarter of the pole sphere as illustrated in Figure 3. For conventional texture spectrometers, the detectors are usually considered as "point-like"; therefore the angular resolution of the resulting texture-related information is determined by the number and grid structure of the measured points on the pole sphere and by the number of (hkl) reflections (pole figures) measured. However, as is obvious from Figure 3, describing each HIPPO detector panel as a point does not accurately describe the coverage. The complicated shape of the panels in pole figure space, over which intensities are averaged, requires a more detailed analysis. It is essential to have a rigorous model of the pole figure coverage to assess the instrument's angular resolution for texture.

As a first step, we analyzed the detector panels from the view of scattering vectors and approximated each panel as a circle with the same area as the actual polygon on the pole sphere. This gives mean detector bank specific diameters of 10.8° (140° bank), 15.9° (90° bank), and 14.0° (40° bank) on a pole figure. In reality, the mean resolution of the 40° bank is worse because of each panel's elongated shape (Figure 3). Thus, even for a single crystal, the peak region in orientation space would have a width of 11-15° at best. The angular resolution *b* for features in a pole figure is approximately given by twice the diameter of these circles (representing the cell size of a regular equal angular grid) and is therefore roughly 25°-30°. In total, the panels of the 3 banks cover about 26% of the pole hemisphere.

The next step was to accurately describe the relationship between panel points in real space, and their positions on the pole sphere (which will depend on the orientation of the sample in the spectrometer). From the design specifications for HIPPO, coordinates of the four corners of each detector panel are given in a right-handed Cartesian coordinate system with the origin at the sample position ('center of the spectrometer'). This coordinate system is henceforth called $\mathbf{K}_H$ and is the spectrometer coordinate system for HIPPO. In this system $+\mathbf{X}_H$ points horizontally towards the beam stop and $+\mathbf{Y}_H$ points vertically upwards; therefore, $+\mathbf{Z}_H$ is horizontal and points towards the right looking along $+\mathbf{X}_H$ (Figure 1). As examples, Table 2 gives the coordinates (in meters) of the center and corners of one detector panel from each bank in $\mathbf{K}_H$.

Pole figures are by definition given in a sample coordinate system $\mathbf{K}_A$. The relationship of $\mathbf{K}_A$ to $\mathbf{K}_H$ for a general sample orientation in the spectrometer requires the definition of a *zero-orientation of the sample*. We define this orientation to be $+\mathbf{X}_A \parallel +\mathbf{X}_H$, and $+\mathbf{Z}_A \parallel +\mathbf{Y}_H$, which leads to $+\mathbf{Y}_A \parallel -\mathbf{Z}_H$. A pole position or direction **y** (unit vector) is given in $\mathbf{K}_A$ by its spherical angles (ϑ_y, φ_y). ϑ_y is the polar angle starting from the north pole at $+\mathbf{Z}_A$, φ_y (azimuth) is the angle from $+\mathbf{X}_A$ towards the projection of **y** onto the ($\mathbf{X}_A$, $\mathbf{Y}_A$) plane rotating $+\mathbf{X}_A$ by a right screw (counterclockwise) around $+\mathbf{Z}_A$. The pole sphere is centrosymmetric due to Friedel's law and we need to describe **y** only in the upper ($Z_A>0$) hemisphere. The corresponding inversion relation for **y**(-) → **y**(+) is $\vartheta_y^+ \rightarrow 180° - \vartheta_y^-$ and $\varphi_y^+ \rightarrow 180° + \varphi_y^-$. In this way all detector panels can be exactly represented in pole figure space (Table 2, Figures 3, 4a). This coverage was incorporated into the computer program GULUWIMV (Matthies, 2002) described in section 4.1. For this study, we used sample rotations of 0°, 45°, 67.5°, and 90° in a right screw around $+\mathbf{Z}_A$ resulting in a 67% coverage of the pole figure (Figure 4c).

For texture representations we use ODF sections in spherical coordinates, relative to the sample coordinate system (gamma sections, using the Matthies/Roe convention for Euler angles) and pole figures. Both are plotted in equal area projection. Calculations and representations have

been made in the same coordinate system as shown in Figure 4c, except for Figure 10, where the ODF was rotated into a more standard orientation of the deformation experiment.

4. Texture analysis of ECAP aluminum

As described above, we have estimated that the angular resolution of HIPPO is on the order of 25-30° for texture measurements. This appears coarse, but is sufficient as long as the textures that are measured are not exceedingly sharp, as is the case for the majority of polycrystalline materials. To test the system with a strong texture typical of deformed metals, we measured equal-channel angular-pressed (ECAP) aluminum. Preliminary investigations indicated that this sample has a clear, sharp and asymmetric texture. The sample has cubic crystal symmetry; triclinic sample symmetry was assumed for the analysis. It was measured for 9 minutes per orientation using the sample changer with four rotations; this yielded 120 spectra. These spectra were the input for all analyses with the exception of GSAS, which can only accept a maximum of 99 spectra. The input spectra are graphically displayed as gray shades in Figure 5. On these "map plots" we immediately observe presence of texture by systematic intensity variations for diffraction peaks. We also recognize some features that need to be addressed in the refinement: The 40° spectra have much better counting statistics but broad diffraction peaks, whereas 140° spectra are weak but display sharp peaks as was discussed in section 2. The background intensity for some spectra is much higher than for others. The main reason for this appears to be that there is preferential high absorption of the beam from the sample holder for detectors that view the specimen from above. Other factors may be detector sensitivity. Some individual tubes may not be operating. These systematic aberrations have to be accounted for in the Rietveld procedure.

In order to compare the results of software packages available for HIPPO texture analysis and to test methodological predictions following from the known angular resolution, the data were analyzed with GULUWIMV (Matthies, 2002) and the Rietveld packages MAUD (Lutterotti *et al*., 1997) and GSAS (Von Dreele, 1997). These approaches include both harmonic and discrete methods.

4.0 Quantities used for ODF comparison

Several scalar quantities S are computed to allow comparison of the ODFs derived with the various approaches. They provide information about the volume fractions within certain ranges of ODF concentrations. The negativity index (NI) is defined as the fraction of the ODF with negative orientation probabilities divided by the fraction with positive values where the total integral over ODF space has been normalized to unity (Matthies, 2002):

$$NI = 100\% \times \frac{\left| \int\limits_{f(g)<0} f(g)dg \right|}{\int\limits_{f(g)>0} f(g)dg} = 100\% \times \frac{|S_-|}{S_+}. \qquad (1)$$

The sum of S_+ and S_- is equal to unity, due to the normalization of the ODF. During analysis with the harmonic method, negative ODF values may appear and cause a corresponding increase of S_+. Therefore, negative values cannot simply be set to zero. This is not a concern for the WIMV methods, where by definition $S_-=0$. A correct ODF will always have NI = 0, because negative probability densities are unphysical. Other useful information from the numerical analysis include the quantities

$$S_{>1} = \int_{f(g)>1} f(g)dg \qquad S_{01} = \int_{0<f(g)<1} f(g)dg \qquad SH_{>1} = \int_{f(g)>1} \big(f(g)-1\big)dg \qquad (2)$$

$S_{>1}$ is the volume fraction of orientations with orientation probabilities higher than random, and S_{01} is the volume fraction between 0 and random, with $S_{>1}+S_{01}=1$ for NI=0. $SH_{>1}$ is the integral above unity (1 m.r.d.) and thus representing the volume of orientations in the "upper world" that is enriched in orientations, as compared to the "lower world" that is depleted in orientations. These values, along with the texture index (F_2) and the minimum and maximum ODF values (f_{min}, f_{max}), are listed in the tables to quantitatively compare the ODFs calculated by the different methods.

4.1 Individual peak method (the GULUWIMV package)

We have used the universal WIMV-related program called GULUWIMV* (Matthies, 2002), which is based on a regular 5° grid. It allows the 'measured' cell grid to be incomplete and with any structure (which may vary for each (hkl)). In other words, the measurements do not need to be arranged in adjoining and completely measured 5°-ϑ-rings (as in the WIMV algorithm of Beartex, Wenk *et al*., 1997), and the measured regions can have the form of 'islands' or contain 'holes' on the pole sphere. This enables us to treat the data from the detector panels as having come from a finite region of pole figure space, rather than a point and to treat the irregular arrangement and form of the HIPPO detectors. A first step maps experimental intensities of measured points (in this case taken from the *.apf file generated by MAUD and already corrected for instrument aberrations; see Section 4.2) from arbitrary panel positions onto the 5° pole figure grid (i.e. Figure 4b). From the number and structure of the 'measured' 5°-cells, the crystal symmetry, and the number and kind of (hkl)-reflections used, GULUWIMV provides information about the number of sample orientations required, in order to get a resolution on the order of b = 25-30°. These conclusions are crystal symmetry dependent. By using the 5°-grid, the appropriate description of the real panel size and shape, and a sufficient number of experimental data, implicit 'deconvolution effects' may conceivably increase the resolution in the derived ODF.

GULUWIMV also has the ability to perform corrections for the intrinsic loss of information when the ODF is derived from pole figures, particularly the "remaining ghost correction step" (Matthies *et al*., 1987) to account for a detected isotropic (random) texture background (phon). This step is less important for highly textured samples where nearly all grains contribute to the texture (low phon); however, for weakly textured samples with a high phon, ghosts may cause the ODF minimum to be lower than the true value with a corresponding increase in apparent texture strength.

GULUWIMV takes as input a series of "pole figures" given by a list of measured diffraction peak intensities as a function of ϑ and φ. For the aluminum sample, we used the seven isolated reflections 111, 200, 220, 311, 222, 400, and 422. The diffraction peak intensities are extracted using the Le Bail method in MAUD (see Section 4.2) after proper corrections and normalizations for diffraction background, incident intensity, and detector efficiency. However, the extracted intensities do not account for overlapping peaks, and well-separated peaks must be used in this approach. For each detector panel, equal intensities are assumed for the pole figure

* GULU Acronym: G – remaining ghost correction; U – universal, any crystal symmetry; L – *Loch* (German – "hole"), any structure of measured cells, allowing "holes" and "islands"; U – *unvollstaendig* (German – "incomplete"), incomplete coverage.

region defined by the four ϑ, φ positions corresponding to the corners of the detector panels (Table 2).

The first iteration of the data through GULUWIMV gives an R_p value (relative error of pole figure fit) of 26.4% with a sharp ODF and zero phon.

$$R_p = \frac{100\%}{I}\sum_{i=1}^{I}\frac{1}{j_i}\sum_{j=1}^{j_i}\frac{\left|P_{\mathbf{h}_i}^{\exp}(\mathbf{y}_j) - P_{\mathbf{h}_i}^{calc}(\mathbf{y}_j)\right|}{P_{\mathbf{h}_i}^{\exp}(\mathbf{y}_j)}, \; (P_{\mathbf{h}_i}^{\exp}(\mathbf{y}_j) > 0.005\,\text{m.r.d.}) \qquad (3)$$

where I is the total number of pole figures ($\mathbf{h}_i$), each with j_i measured pole figure positions ($\mathbf{y}_j$) (Matthies *et al*., 1988). Only pole densities greater than 0.005 m.r.d. are included in the calculation of Rp. Experimental pole figures are indicated with a superscript exp, while the recalculated are given with superscript calc. Figure 6a shows some gamma sections of the ODF in the vicinity of the main texture component. While the ODF has a minimum of zero, there is likely some isotropic component that is obscured by ghosts. We choose the minimum value from the normalized experimental pole figures as an initial guess for the phon. The input phon is then reduced until an ODF can be calculated with the input phon as a minimum. This is the "remaining ghost correction."* With a phon of 0.07, the R_p improves to 26.1% (Figure 6b). The small improvement in R_p and small phon shows that the sample is strongly textured and nearly all grains contribute to the main texture component.

The resulting ODF is smoothed with g = 7.5° Gaussians to overcome the discrete 5°-cell effects. Finally, a g = 10° Gauss filter is applied (much smaller than the discussed resolution of 25-30°) to remove remaining stochastic noise while maintaining the texture strength F_2. The final ODF (Figure 6c) has a texture index (F_2) of 3.37 m.r.d.^{2}, f_{min} = 0.11 m.r.d., and f_{max} = 14.13 m.r.d. (Figure 6c). Because this technique is able to perform the remaining ghost correction and incorporate the real form of the HIPPO detectors, we accept in this study the ODF produced by GULUWIMV as a reference and compare it in Table 4 with ODFs generated by the other methods.

An additional subroutine in GULUWIMV computes harmonic coefficients from the discrete ODF and can reconstruct an ODF and pole figures from the standardized harmonic coefficients. We calculated both l = even and l = odd harmonic coefficients (C_{lmn}) for l up to L = 12 from the ODF of Figure 6c (where L is the maximum order of the harmonic expansion). The harmonic methods of texture analysis from pole figures can not generate the l = odd terms (Mattthies, 1979). In the cubic case for L = 12 the only odd coefficients that are not identical to zero are for l = 9. Therefore we removed the l = 9 terms to create a reduced ODF $\widetilde{f}(g)$ that can be compared to that of conventional harmonic methods implemented in the Rietveld codes GSAS and MAUD (Figure 6d). Rows d to f in Table 4 show that the ODF using all coefficients, f(g), is more similar to the ODF from the WIMV method than is the ODF constructed from only

---

* Due to the loss of ODF information by normal scattering (Friedel's Law) only a "reduced" ODF $\widetilde{f}$(g) can be reconstructed unambiguously from reduced pole figures. $\widetilde{f}$ (g) may be negative for some orientations g and contains significant artifacts (ghosts). A first ghost correction ($f(g) \geq 0$) follows automatically from WIMV-like algorithms. However, for a large isotropic background (f_{min} = "phon"; $0 \leq$ phon ≤ 1) in the real ODF, there may be several ODF-solutions that can explain the experimental data. The WIMV concept attempts to find the solution with the highest phon and texture index (F_2). This step is called the remaining ghost correction (Matthies & Vinel, 1982).

even coefficients, $\widetilde{f}(g)$. The f_{max} and the texture index (F_2) are both reduced significantly due to harmonic series truncation effects. Without the $l = 9$ terms, the negativity index (NI) becomes 0.8%. The calculation of the odd terms of the spherical harmonics coefficients is only possible due to the "knowledge" of the ODF from the WIMV algorithm.

We choose L = 12 based on our estimate of the resolution, b = 30° by applying the 'L360' rule of thumb:

$$\mathrm{L360} \equiv 360° / b(°) \tag{4}$$

(Matthies, 2002); b is the texture resolution defined above. A harmonic series truncated at L360 is able to separate at best two texture peaks b(°) apart. This rule follows from the distance d°=180°/L of the zero points for the elementary harmonic functions $\sin(L\varphi)$ or $\cos(L\varphi)$, characterizing the effective minimum cell size for a given L in the φ-space (0°≤ φ ≤360°). For example for L=4 it follows that d°=45. Consequently using such cells (columns), peaks with halfwidths (FWHM) b≥2d°=90° (Matthies, 1982) will be sufficiently described in the φ–space by harmonic series with l up to L. Therefore L = 12 or at best 14 harmonic series for data from HIPPO is reasonable from a methodological point of view. Increasing L beyond 14 will not improve the results in the case of fit procedures, due to inconsistencies between the point-like consideration of the panels and their real form and sizes.

4.2 Rietveld with MAUD-EWIMV

MAUD uses the Rietveld method, originally developed to determine crystal structures from powder samples by fitting the complete measured diffraction spectra and refining instrument, phase, and sample parameters. Because it uses the whole spectra, it can also account for overlapping peaks. All spectra (Fig. 5) were taken as input, though only the information within the computation range (0.8Å-2.6Å) was used, yielding 204,400 data points. Instrumental, background, and phase parameters were refined.

Instrumental parameters were first calibrated using a Si powder standard (NIST SRM-640c), and are used to fit the instrumental peak aberrations that are convoluted with peak broadening due to the sample (e.g. crystallite size, microstrain and microstructure). It is necessary to extract the peak broadening parameters with a well-defined standard and then keep instrument parameters fixed, in order to accurately extract microstructural information from the unknown sample. For each bank an overall intensity factor was refined. In addition, for each detector of a bank (and constant for all rotations) a scale factor was refined to take account of detector efficiency and variations in absorption as illustrated e.g. on the map plots in Figure 5 with intensity variations that affect both background and peak intensities. These scale factors vary from 0.4 to 1.3. Two sample displacement parameters (Y and Z, in mm) were refined to take account of the fact that the sample was not exactly aligned in the goniometer rotation axis. It was found that the misalignment is about 0.5 mm. These instrumental parameters are assumed to be constant for all sample orientations measured with the same detector. We refined background parameters for each spectrum individually. The lower angle detectors have a more complex background after being normalized by the incident intensity function and 2, 3, and 4 parameters were used for each spectrum from the 140°, 90° and 40° banks, respectively. The background function is a polynomial corrected with the incident spectrum.

Once the background and instrument parameters were refined, we refined crystallographic parameters such as the lattice parameter a and isotropic thermal parameter (U_{iso}) as well as effective crystallite size (This is the size of the average coherently scattering domain

that may be different from the microstructural grain). In the case of ECAP aluminum the crystallites were sufficiently large (around 1 μm) to cause insignificant additional peak broadening. At this point in the refinement we obtained R_w = 14.1%. R_w is the weighted mean error over all spectral data ($w_i = 1/I^{exp}$ weights during fit, exp experimental, calc recalculated):

$$R_w(\%) = 100\% \sqrt{\frac{\sum_{\substack{all\ spectra,\\ all\ channels}} w_i \left(I_i^{\exp} - I_i^{calc}\right)^2}{\sum_i w_i (I_i^{\exp})^2}} \quad (5)$$

The peak intensities were extracted by the Le Bail method (Le Bail et al., 1988) and used as input for the GULU chain of programs as described above. The results of the refinement of the instrumental, background and phase parameters served then also as the basis of the texture calculations in MAUD. In total, 384 parameters are refined simultaneously of which 376 are background parameters for the 120 spectra. Table 3 lists some refined crystallographic parameters.

MAUD contains a WIMV-related texture algorithm called E-WIMV. As for all WIMV-like direct algorithms, in E-WIMV all ODF values are positive numbers, avoiding the problem of unphysical negative orientation frequencies. However in E-WIMV the "remaining ghost corrections" (i.e. taking the randomly oriented background into account, as done in GULU) is in part assured by the entropy-like algorithm that assures "the smoothest solution", thus maximizing the background. There is no explicit consideration of the detector size and shape but an implicit correction is done with the larger cell size adopted and the "tube projection" feature that provides also direct smoothing of the ODF. In MAUD, "arbitrary" point-like measuring grids can be considered, avoiding the interpolation step. The experimental data at arbitrary positions in pole figure space are used to compute the tube projection path in the ODF of the corresponding (user specified) cell size. To conform to the actual instrument resolution we chose an ODF cell size of 10° and to obtain additional smoothing we choose a tube projection radius of 20°. This means that all ODF cells which are within 20° from the true integration path are being considered. They are weighted proportionally to the reciprocal distance from the integration path. MAUD uses the entire spectrum inside the computation range for texture analysis (in this case, d = 0.8-2.6 Å resulting in 9 usable reflections). In addition in MAUD-E-WIMV each pole figure is weighted in the analysis based on its intensity (the weights are computed as the classical square of the intensity) so that also the weak peaks can be used and the correct statistical errors are taken into account in the ODF determination.

In the present version, MAUD assumes that the measured intensities correspond to the centers of the detectors; however, some consideration of angular resolution is achieved by selecting an appropriate ODF cell size and tube projection but uniform for all detectors despite their real size. After refining the texture (E-WIMV), the overall fit improved to R_w = 8.19%. The numerical results of the ODF for both the unfiltered and filtered ODF are listed in Table 4. The f_{max} for the raw ODF is 28.7, which is lower than the result from GULUWIMV of 62.7. The MAUD ODF can be further smoothed and filtered in BEARTEX (Wenk et al. 1997) exactly as was done for the GULUWIMV ODF (Figure 7c). After applying smoothing and filtering, f_{max} drops to 21.0. Comparing the filtered MAUD ODF with the filtered GULUWIMV ODF, the MAUD ODF has a higher maximum and texture index, which is often used to say that it has a

stronger texture. However, the fraction of grains above 1 m.r.d. ($SH_{>1}$) is the same for both ODFs and MAUD actually has a lower $S_{>1}$ value, indicating that fewer grains are contributing to the peak than in the GULUWIMV ODF. Therefore, differences in the two ODFs indicate that, while similar, the MAUD ODF has slightly narrower texture peaks, even though the volume of the main texture component (above 1 m.r.d.) is the same as in the GULUWIMV ODF. This produces a sharper peak that skews the maximum and the texture index and is due to stochastic effects in the discrete representation. It is worth pointing out that, while most attention is usually paid to the texture peaks, in both ODFs, the "lower world" below 1 m.r.d. contains almost half of all orientations (Table 4). Pole figures were recalculated from the filtered MAUD ODF and are shown in Figure 8b and compared with the GULUWIMV pole figures (Figure 8a); the corresponding numerical information is summarized in Table 5. It should be noted that numbers such as ODF and pole figure maxima are highly influenced by smoothing procedures, which are fairly arbitrary.

As we did for the ODF from GULUWIMV, we converted the MAUD ODF into harmonic coefficients and found a similar relationship between the ODF from direct methods and the harmonic ODFs discussed in the next sections.

4.3 Rietveld with MAUD-harmonic method

MAUD also has the capability to determine the ODF with the harmonic method, though the harmonic method is computationally slower than E-WIMV. The even order spherical harmonics coefficients are refined as part of the Rietveld refinement. We selected L = 12, which generates 110 (even) coefficients for the given case of cubic crystal symmetry and no sample symmetry. The coefficients were refined along with the background, incident intensity, and lattice and thermal parameters as was described in section 4.2. The lattice parameter and thermal parameter are given in Table 3. They agree closely with the E-WIMV parameters. This refinement yielded a similar fit to the spectra with R_w = 8.8%. Though this method is independent of the E-WIMV method, the even tesseral C_{lmn} coefficients resulting from the direct refinement and those recalculated from the E-WIMV ODF are very similar. The even ODFs and pole figures determined by the harmonic method have negative regions (Figure 7c and Figure 8c).

The resulting ODF has a negativity index of 4.2% and significant negative regions appear near the main texture component (Figure 7c). Pole figures are almost entirely positive (Figure 8c, Table 5). Again, as in the harmonic ODFs calculated from GULUWIMV, the maximum is depressed and the minimum falls to negative values. The S_+ intensity of the ODF is now equal to 1.04, showing the distortion caused by the presence of negative values. It becomes difficult to compare the other values in Table 4 because the positive part of the MAUD harmonic ODF is 4% larger, containing 4% more "grains", than the discrete ODFs with $S_+ \equiv 1$.

Table 6 lists the results of the harmonic method in MAUD for different order of expansion, L = 6-22. These results came from using the starting refinement described in section 4.2 and then refining with the harmonic coefficients for 3 iterations (enough for the weighted sum of squares to stabilize). Table 6 illustrates that with increasing order R_w decreases and F2 increases. Beyond L=12 NI rapidly increases, indicating that the solution is unstable and no meaningful texture information is added. This supports our previous conclusions that for the HIPPO detector geometry and coverage L=12 is optimal. It is interesting to note that with increasing order negative regions become more pronounced and thus they are not series termination effects. The reason why R_w decreases with order is not an indication for a better

texture solution but simply indicates a better least squares fit to the data due to a larger number of free fit parameters.

4.4 Rietveld with GSAS-harmonic method

GSAS is the original LANSCE Rietveld program for determining crystal structures (Larson & Von Dreele, 2004) that has been modified to obtain texture information by applying the harmonic method (Von Dreele, 1997). Together with fitting the measured spectra using sample, phase, and instrument parameters, GSAS uses a harmonic model to fit the remaining intensity variation caused by texture in the sample. GSAS can accept at most 98 spectra (histograms) as input (99 when not incorporating a "positive pole figure restraint" (p. 172 of Larson and Von Dreele, 2004), which drives the refinement to positive pole figure values). We used 98 out of the 120 available spectra and the zero pole figure constraint, leaving out some low resolution data from the 40º banks. In our refinement strategy, the background and histogram scale factors are refined first. We use a power series in $n!/Q^{2n}$ to model the shape of the incident beam with 4 terms per spectrum and a background damping factor of 4. This step includes 490 total parameters in the refinement. The program is then set to the Le Bail mode and the background and scale factors are fixed to refine the lattice parameter and, for each spectrum, the profile coefficients RSTR and σ_1 that account, respectively, for a potential slight histogram dependent shift in the peak position due to sample misalignment and for the peak width (Von Dreele et al., 1982). This refinement includes 197 parameters. Returning to Rietveld mode, lattice parameter, RSTR, and σ_1 parameters were fixed for the remaining refinement and we refined the background parameters and histogram scale factors with U_{iso} (isotropic thermal parameter, Table 3) before introducing the positive pole figure restraint to refine the harmonic texture coefficients. In the end $R_w = 6.24\%$ with 166,488 observations used for d = 0.8Å - 2.62Å (10 msec in TOF).

As in MAUD, GSAS does not take the shape of the panels into account when fitting the texture. Pole figures are recalculated from the spherical harmonics coefficients. For our sample and L = 12, these pole figures appeared similar to the GULUWIMV and MAUD EWIMV results, though significant negative areas were visible, for instance in the 111 pole figure with min = -0.14, max = 4.06 (Table 5), even with the "positive pole figure restraint". BEARTEX pole figure output in GSAS truncated negative values without renormalizing the pole figures. The truncated pole figures are difficult to interpret quantitatively due to the missing normalization. Also, GSAS does not provide a numerical output of the ODF. We therefore used a different method for comparison by first obtaining an ODF from the GSAS generated fit-coefficients.

GSAS lists refined harmonic coefficients that are related but not equivalent to the normalized C_{lmn} coefficients as defined in the classic harmonic method (Bunge, 1982, Matthies et al. 1987). We were able to determine a relationship between the symmetrized coefficients of MAUD and BEARTEX (related to symmetrized spherical 'tesseral' functions, Matthies *et al*., 1987, see also MacRobert and Sneddon, 1967) and the GSAS coefficients (related to the R_{2l}^{μ} functions used by Popa, 1992). The third index of the GSAS coefficient is the same as the μ (2^{nd}) index. The tesseral $\overline{n}(\nu)$ coefficients are linear sums and differences of the GSAS coefficients with positive and negative 2^{nd} indices. The zero term is the same for both. This is illustrated for the $l = 4$ terms in Table 7.

However, this simple correlation is only applicable for the cubic case and only for $l<12$. When we input the coefficients resulting from our transformation for L = 12 into Beartex, we obtain an ODF and can recalculate pole figures that look very similar to the L = 12 pole figures from MAUD (Figure 8d, Table 5). The numerical analysis of this ODF is included in Table 4 for comparison with other methods.

6. Discussion and Recommendations

With the successful texture analysis of the round-robin sample of limestone (Wenk *et al*. 2003) it was demonstrated that the new HIPPO diffractometer at LANSCE is capable of measuring textures quantitatively and efficiently. This new comparative analysis demonstrates that quantitative results are also obtained for much sharper textures but with limitations that depend on the analytical method. It was also reassuring to see that different methods of texture analysis provide similar results. GULUWIMV is able to account for the true form of the detectors. At this point the method can only be used for well-separated diffraction peaks, or for perfectly overlapped peaks, for which relative intensity contributions are known based on structure factors. Also, another method must be used to extract and correct the integrated intensities from the spectra.

For direct methods in the Rietveld scheme, E-WIMV in MAUD provides resolution ranges from 2.5º to 30º. In the case of the current configuration of HIPPO, the angular width of a detector panel is approximately 15º and is the limiting constraint for the angular texture resolution of 25-30°. This is to some extent governed by the binning scheme and could conceivably be changed by software in the future. Texture results for E-WIMV in MAUD and GULUWIMV are very similar. General advantages of the Rietveld method over the use of individual peak intensities are that results are less subject to systematic errors and problems with peak shape and overlaps, because the solution is constrained by a physical model, allowing fewer degrees of freedom. It also allows refinement of structural and microstructural parameters such as lattice parameters, atomic coordinates, temperature factors, and crystallite size.

The results from the harmonic methods, both in MAUD and GSAS illustrate the well-known limitations: termination errors and lack of odd coefficients, in addition to restrictions imposed by irregular and limited pole figure coverage. Both Rietveld programs do incorporate any of the sophisticated approaches to extract odd coefficients (e.g. Dahms & Bunge 1988, Van Houtte 1991). Even though computationally straightforward it turns out that limited detector resolution and irregular data coverage are much more serious for harmonic than discrete methods as was already established earlier (Xie et al. 2003). Using L = 12 (b=30º) or 14 (b=25º) is reasonable from a methodological point of view. Interestingly, increasing L does not improve results as it does for conventional pole figure goniometer analysis where the expansion is usually carried to L=32. This is demonstrated by values in Table 6 with considerable negative values beyond L=12 and unrealistic oscillations (Figure 8). We further emphasize this with Figure 9 that shows 100 pole figures, contouring only the region below 1 m.r.d. From Table 4 we concluded that even for this strong texture this region below 1 m.r.d. contains about one third of all orientations.

Figure 9a is the 100 GULUWIMV pole figure with a very smooth topography and a symmetrical peak shape (white region). The corresponding MAUD-E-WIMV pole figure is almost identical. GSAS pole figures are shown for L=12, 14 and 16. For L=12 and 14 the topography is relatively stable but with additional maxima and minima that we attribute to series termination effects. For L=16 the pattern becomes unstable with numerous oscillations. This

worsens with increasing L. Thus the harmonic method clearly defines the resolution of HIPPO as 25º at best. This has also been found in earlier neutron diffraction studies with similar detectors for examples of rocks (Wenk *et al*., 2001) and coins (Xie *et al*., 2004). For any quantitative description of texture this "lower world" of texture information, highlighted in Figure 9, is equally important as the "upper world" and obviously direct methods have an advantage and provide a more realistic representation. Negative values are meaningless in ODFs and pole figures and influence the positive values as well, because of normalization. In our comparisons, we observe that only the WIMV-related algorithms were able to give non-negative ODFs. The harmonic method in GSAS and MAUD produce the same pole figures and ODFs, establishing that formally both methods are correct within the harmonic frame, even though different implementations are used.

Having analyzed in detail the resolution of the HIPPO diffractometer for the analysis of a very strongly textured sample and discussed advantages and disadvantages of different methods for obtaining orientation distributions, it is now appropriate to briefly compare HIPPO textures with those obtained by other methods. Also, we would like to relate the measured texture to deformation conditions in the channel die extrusion experiment. The pole figures and ODFs illustrated in the previous sections are highly asymmetric which was suitable for the texture analysis but difficult to interpret. Metallurgists would like to view the pole figures in the plain strain geometry of the experiment, with the transverse direction in the center and the shear plane oriented NE-SW. For this we rotate the orientation distribution according to established angular transformations provided by the instrument scientist: first a -61.7º rotation around the vertical axis (center of pole figure) to account for the displaced origin in the HIPPO sample changer, then a 90º rotation around the new top axis (Fig. 10a-c). It is surprising that there is still considerable asymmetry, but we recognize a 001 concentration close to the shear plane normal (SPN) and a 110 concentration near the shear direction (SD).

On the same sample, we measured the texture by electron backscatter diffraction (EBSD) on the Berkeley system and obtained pole figures in Figure 10d-f. They are much more symmetrical with respect to the channel die geometry, but it is satisfying to see that pole densities and texture peak widths are very similar as those determined by neutron diffraction. The 25-30º HIPPO resolution was not a limiting factor for this particular texture. A major weakness of the HIPPO neutron diffraction experiment is that the orientation of the specimen in the sample chamber is poorly defined and arbitrary rotations of over 25º are required to bring the HIPPO pole figures (Figure 10 a-c) to coincidence with EBSD pole figures (Fig. 10 d-f). Clearly such ambiguities are of major concern for mechanical interpretations and for quantitative texture analysis great care should be devoted to establish an accurate and strictly reproducible sample orientation relative to beam and detector coordinates.

The texture of the ECAP sample can then be described as more or less a single {001}<110> component which has been observed in fcc metals with high stacking fault energy deformed in torsion and was modeled with the relaxed Taylor theory (Canova et al. 1984) as well as the viscoplastic self-consistent approach (Hughes et al. 2000) for high strain simple shear deformation. While this sample was a good test for comparing analytical methods for TOF texture analysis, it is obvious that neutron diffraction has no particular advantage for such samples over X-ray diffraction and EBSD that provide immediate results with minimal efforts.

6. Conclusions

We have shown that the HIPPO diffractometer at LANSCE is capable of quantitative texture analysis as long as the features of interest are not sharper than the angular resolution of the instrument. Determining this resolution to be 25°-30° was first established by knowing the actual sizes and layout of the detector panels and then confirmed by the analysis, particularly the harmonic method that can not be extended beyond L=12. It may be possible to improve the resolution somewhat by incorporating the information from a larger number of diffraction peaks and rotating the sample in an optimized set of rotations. This optimization will depend on the crystal symmetry and the detector panels used in the experiment. In this study, with a cubic phase, we found good results using only four rotations and measuring for only 9 minutes per orientation. The layout of the HIPPO detector panels allows adequate coverage to be obtained by rotating the sample around a single axis. This feature has facilitated the development of a host of ancillary equipment for measuring texture *in situ* under conditions of temperature, stress, or pressure.

The example of ECAP aluminum further establishes direct methods within the Rietveld scheme as an elegant and quantitative way to obtain texture information from neutron TOF spectra measured with multidetector systems. With more samples that are analyzed, more experience will be gained and no doubt algorithms will be refined and standardized. The harmonic method within the Rietveld scheme and for the HIPPO instrument is adequate for a qualitative survey of principal textural features and may be used as a texture correction for crystallographic refinements, but it should not be used for quantitative texture analysis.

We conclude by emphasizing that HIPPO is ready for quantitative texture analysis, even of strongly textured samples. Naturally for the two test examples that we have studied in detail, experimentally deformed limestone with a weak texture (Wenk et al. 2003) and ECAP extruded aluminum, neutron diffraction would not have been necessary to determine the texture and users should employ this instrument for applications where TOF neutrons and Rietveld texture analysis have unique advantages, such as low symmetry and composite materials with complex diffraction spectra, in situ observation of texture changes at non-ambient conditions and materials of coarse grain size that require large sample volumes.

Acknowledgements: We appreciate discussions and help from R. Von Dreele and I. Huensche. David Alexander and Saiyi Li kindly provided the sample used in this study. The research has been supported by IGPP-LANL, CLE-UCOP and NSF. Experiments were conducted at the Los Alamos Neutron Science Center at Los Alamos National Laboratory. LANSCE is funded by the US Department of Energy under contract W-7405-ENG-36.

References

Bunge, H.-J. (1982). *Texture Analysis in Materials Science – Mathematical Methods*. London: Butterworths.

Canova, G.R., Kocks, U.F. and Jonas J.J. (1984). *Acta metal*. **32**, 211-226.

Dahms, M. & Bunge, H. J. (1988). *Textures and Microstructures* **10**, 21-35.

Hughes, D.A., Lebensohn, R.A., Wenk, H.-R. and Kumar, A. (2000). *Proc. Roy. Soc. London* **456**, 921-953.

Ino, T., Ooi, M., Kiyanagi, Y., Kasugai, Y., Maekawa, F., Takada, H., Muhrer, G., Pitcher, E. J., & Russell, G. J. (2004). *Nucl. Instr. Methods Phys. Res. A* **525**, 496-510.

Larson, A. C. & Von Dreele, R. B. (2004). *General Structure Analysis System (GSAS)*. Los Alamos National Laboratory Report LAUR 86-748.

Le Bail, A., Duroy, H. & Fourquet, J. L. (1988). *Mat. Res. Bull.* **23**, 447-452.

Lokshin, K. A., Zhao, Y. S., He, D. W., Mao, W. L., Mao, H. K., Hemley, R. J., Lobanov, M. V. & Greenblatt, M. (2004). Phys. Rev. Lett. **93**, 125503.

Lutterotti, L., Matthies, S., Wenk, H.-R., Schultz, A. J. & Richardson, J. W. (1997). *J. Appl. Phys*. **81**, 594-600.

MacRobert, T. M. and Sneddon, I. N. *Spherical Harmonics: An Elementary Treatise on Harmonic Functions, with Applications, 3rd ed. rev.* Oxford, England: Pergamon Press, 1967.

Matthies, S. (1979). *Phys. stat. Solidi* B**92**, K135-138.

Matthies, S. (1982). *Aktuelle Probleme der Quantitativen Texturanalyse*. Zentralinstitut fuer Kernforschung, DDR, ZFK-480. ISSN 0138-2950.

Matthies, S. (2002). *Proc. ICOTOM-13*. Trans. Tech. Publications. pp 95-100.

Matthies, S., Lutterotti, L. & Wenk, H.-R. (1997). *J. Appl. Cryst.* **30**, 31.

Matthies, S. & Vinel, G. W. (1982). *Phys. Status Solidi* B**112**, 111-120.

Matthies, S., Vinel, G. W. & Helming, K. (1987). *Standard Distributions in Texture Analysis*. Volume 1. Berlin: Akademie-Verlag.

Matthies, S., Wenk, H.-R. & Vinel, G. W. (1988). *J. Appl. Cryst.* **21**, 285-304.

Popa, N. C. (1992). *J. Appl. Cryst.* **25**, 611-616.

Roberts, J. A. (1999). The Los Alamos Neutron Science Center (LANSCE), *Neutron News*, **10** (4), 11-14.

Rodriguez, M. A., Ingersoll, D., Vogel, S. C. & Williams, D. J. (2004*). Electrochem. and Solid-State Lett.* A**7**, 8.

Rollett, A. D. & Wright, I. (1998). *Texture and Anisotropy*. Edited by U. F. Kocks, C. N. Tomé, & H.-R. Wenk, pp. 178-239. Cambridge University Press.

Van Houtte P. (1991). *Textures and Microstructures* **13**, 199-212.

Von Dreele, R. B. (1997). *J. Appl. Cryst*. **30**, 577-587.

Von Dreele, R. B., Jorgensen, & Windsor (1982). *J. Appl. Cryst.* **15**, 581-589.

Vogel, S. C., Hartig, C., Lutterotti, L., Von Dreele, R. B., Wenk, H.-R. & Williams, D. J. (2004). *Powder Diffraction* **19**, 65-68.

Walther, K., Ullemeyer, K., Heinitz, J., Betzl, M. & Wenk, H.-R. (1995). *J. Appl. Cryst*. **28**, 503-507.

Wenk, H.-R. (1991). *J. Appl. Cryst.* **24**, 920-927.

Wenk, H.-R., Cont, L., Xie, Y., Lutterotti, L., Ratschbacher, L. & Richardson, J. (2001). *J. Appl. Cryst.* **34**, 442-453.

Wenk, H.-R., Lonardelli, I. & Williams, D. (2004). *Acta Mater.* **52**, 1899-1907.

Wenk, H.-R., Lutterotti, L. & Vogel, S. (2003). *Nucl. Instr. Methods A***515**, 575-588.
Wenk, H.-R., Matthies, S., Donovan, J. & Chateigner, D. (1997). *J. Appl. Cryst*. **31**, 262-269.
Xie, Y., Lutterotti, L., H.R. Wenk and F. Kovacs (2004). *J. Materials Science* **39**, 3329-3337.

Tables

Table 1. Detector specifications for HIPPO. The d ranges are for 0.5-9 Å wavelength range and the d-range resolution $\Delta T/T = \Delta d/d$ is full width at half maximum over position. Numbers in parentheses are the panel numbers of the detectors in that bank. Only panels 1-30 are typically used in texture experiments.

Bank name	**no. panels**	**d range (Å)**	**resolution**
2θ = 140º	8 (1-8)	0.15-4.90	0.37%
90º	10 (9-18)	0.20-6.33	0.74%
40º	12 (19-30)	0.40-12.67	1.8%
20º	12 (31-42)	0.65-26.1	4.6%
10º	8 (43-50)	1.19-47.5	9.2%
Total	50		

Table 2. Locations of the corners and center of one detector panel from each bank given in the sample coordinate system (K_A) for the zero position of the sample and in the spectrometer coordinate system (K_H). See the text for a further definition of the coordinate systems used.

Panel Number	Corner Number	in K_A ϑ_y (°)	φ_y (°)	in K_H x (m)	y (m)	z (m)	Bragg 2θ (°)
1	1	68.98	173.11	-0.965	0.894	-0.279	135.85
1	2	76.60	174.39	-0.965	0.495	-0.203	151.00
1	3	76.60	185.61	-0.965	0.894	0.279	151.00
1	4	68.98	186.89	-0.965	0.894	0.279	135.85
1	center	72.13	180.00	-0.965	0.695	0.000	144.26
9	1	76.36	143.08	-0.181	0.320	-0.792	101.97
9	2	63.41	150.51	-0.181	0.596	-0.586	102.22
9	3	56.29	139.00	0.181	0.596	-0.586	77.78
9	4	73.08	131.15	0.181	0.320	-0.792	78.03
9	center	66.96	140.21	0.000	0.458	-0.689	90.00
19	1	27.36	148.69	0.749	0.760	-0.203	46.24
19	2	23.05	141.08	1.105	0.760	-0.203	35.47
19	3	23.05	218.92	1.105	0.760	0.203	35.47
19	4	27.39	211.06	0.749	0.760	0.203	46.41
19	center	19.66	180.00	0.9270	0.760	0.000	39.32

Table 3. Crystallographic parameters.

	a Å	U_{iso}
MAUD E-WIMV	4.04529(2)	0.01395(6)
MAUD harmonic	4.04527(2)	0.01319(6)
GSAS	4.05922(3)	0.01259(6)

Table 4. Comparison of ODFs for ECAP aluminum, calculated using MAUD, GSAS, and GULUWIMV packages. (a) GULUWIMV from 7 pole figures without remaining ghost correction, smoothing, or filtering. (b) GULUWIMV after remaining ghost correction of 0.07 m.r.d. (c) GULUWIMV with remaining ghost correction and 7.5° smoothing. (d) GULUWIMV with remaining ghost correction, 7.5° smoothing, and 10° filter. (e-f) L=12 Harmonic coefficients calculated from (d) with and without *l* = odd terms. (g) MAUD E-WIMV without smoothing or filtering. (h) MAUD E-WIMV with 7.5° smoothing. (i) MAUD E-WIMV with 7.5° smoothing and 10° filter, no remaining ghost correction. (j-k) L=12 Harmonic coefficients calculated from (h) with and without *l* = odd terms. (l) MAUD harmonic method, L = 12. (m) GSAS L=12. Values used in the table are explained in Section 4.0.

			f_{min} (mrd)	f_{max} (mrd)	F_2 (mrd^2)	S_+	S_-	S_{01}	$S_{>1}$	$SH_{>1}$	NI
a	GULU raw	$f(g)$	0.00	61.6	7.07	1.00	0.00	0.23	0.77	0.54	0.0%
b	GULU gc	$f(g)$	0.07	62.8	6.74	1.00	0.00	0.26	0.74	0.53	0.0%
c	GULU smooth	$f(g)$	0.10	20.7	3.37	1.00	0.00	0.34	0.66	0.41	0.0%
d	GULU filtered	$f(g)$	0.11	14.1	3.37	1.00	0.00	0.35	0.65	0.41	0.0%
e	Harmonic from d	$f(g)$	-0.02	10.6	2.82	1.00	0.00	0.37	0.63	0.39	0.0%
f	Harmonic from d	$\widetilde{f}(g)$	-0.33	9.48	2.75	1.01	-0.01	0.30	0.70	0.41	0.8%
g	MAUD raw	$f(g)$	0.08	28.7	5.39	1.00	0.00	0.35	0.65	0.43	0.0%
h	MAUD smooth	$f(g)$	0.11	23.5	4.04	1.00	0.00	0.38	0.62	0.39	0.0%
i	MAUD filtered	$f(g)$	0.14	21.0	4.04	1.00	0.00	0.39	0.61	0.41	0.0%
j	Harmonic from i	$f(g)$	0.05	12.4	3.12	1.00	0.00	0.41	0.59	0.39	0.0%
k	Harmonic from i	$\widetilde{f}(g)$	-0.38	11.1	3.01	1.01	-0.01	0.29	0.72	0.42	1.1%
l	MAUD harmonic	$\widetilde{f}(g)$	-1.02	10.9	3.11	1.04	-0.04	0.23	0.81	0.46	4.2%
m	GSAS harmonic	$\widetilde{f}(g)$	-1.15	11.0	3.21	1.05	-0.05	0.23	0.82	0.47	5.0%

Table 5. Comparison of recalculated pole figures for ECAP aluminum. Pole figures recalculated from (a) GULUWIMV with remaining ghost correction, 7.5^o smoothing, and 10^o filter. (b) MAUD E-WIMV with 7.5° smoothing and 10° filter. (c) MAUD harmonic method L = 12. (d) GSAS L = 12.

		max (mrd)	min (mrd)	max (mrd)	min (mrd)	max (mrd)	min (mrd)
		100		110		111	
a	GULU	5.75	0.24	2.91	0.20	4.03	0.23
b	MAUD	6.52	0.27	3.36	0.30	4.48	0.24
c	MAUD	5.13	0.05	2.92	0.01	3.76	-0.02
d	GSAS	5.46	-0.12	2.72	0.07	4.06	-0.14

Table 6. Comparison of harmonic ODFs, $\widetilde{f}(g)$, from MAUD for orders 6-22. Quantities used are described in Section 4.0. N is the number of harmonic coefficients.

order	N	R_w	f_{min} (mrd)	f_{max} (mrd)	F_2 (mrd^2)	S_+	S_-	S_{01}	$S_{>1}$	$SH_{>1}$	NI
6	22	10.5%	-1.00	6.01	2.36	1.04	-0.04	0.26	0.78	0.42	3.8%
8	39	9.8%	-0.82	7.66	2.59	1.05	-0.05	0.23	0.82	0.43	4.4%
10	60	9.2%	-0.97	8.73	2.64	1.04	-0.04	0.26	0.78	0.42	3.4%
12	110	8.8%	-1.02	10.9	3.11	1.04	-0.04	0.23	0.81	0.46	4.2%
14	139	8.5%	-1.22	11.9	3.33	1.07	-0.07	0.24	0.83	0.47	6.1%
16	205	8.3%	-1.91	11.8	3.48	1.08	-0.08	0.21	0.87	0.49	7.7%
18	279	8.1%	-2.60	12.8	3.63	1.10	-0.10	0.20	0.91	0.52	9.4%
20	361	7.8%	-2.82	12.7	3.81	1.14	-0.14	0.19	0.95	0.54	12.0%
22	451	7.5%	-2.79	14.1	4.09	1.17	-0.17	0.16	1.01	0.59	14.4%

Table 7. Relationship between symmetrized (tesseral) harmonic indices $C_{l\mu\nu}$ used in MAUD and BEARTEX, and harmonic indices C_{lmn} used in GSAS for $l = 4$. ECAP aluminum (cubic crystal symmetry and triclinic sample symmetry). Compare the MAUD values and mixing results.

MAUD Clμν	$\overline{n}(\nu)$	GSAS Clmn -mix	GSAS Clmn	GSAS value	MAUD value	Mixing result
C_{411}	0	C_{401}	C_{401}	-1.192	-1.152	-1.192
C_{412}	-1	$-C_{4\text{-}11} + C_{411}$	$C_{4\text{-}11}$	0.473	-1.464	-1.428
C_{413}	+1	$C_{4\text{-}11} + C_{411}$	C_{411}	-0.956	-0.543	-0.483
C_{414}	-2	$-C_{4\text{-}21} + C_{421}$	$C_{4\text{-}21}$	-0.583	0.154	0.149
C_{415}	+2	$C_{4\text{-}21} + C_{421}$	C_{421}	-0.434	-1.187	-1.017
C_{416}	-3	$-C_{4\text{-}31} + C_{431}$	$C_{4\text{-}31}$	0.039	1.457	1.363
C_{417}	+3	$C_{4\text{-}31} + C_{431}$	C_{431}	1.402	1.544	1.440
C_{418}	-4	$-C_{4\text{-}41} + C_{441}$	$C_{4\text{-}41}$	-0.062	0.198	0.236
C_{419}	+4	$C_{4\text{-}41} + C_{441}$	C_{441}	0.175	0.153	0.113

Figures

Figure 1. Schematic view of the HIPPO diffractometer with 5 rings of detector panels. Axes indicate the spectrometer coordinate system $\mathbf{K}_H$. Panel numbers follow those in Table 1.

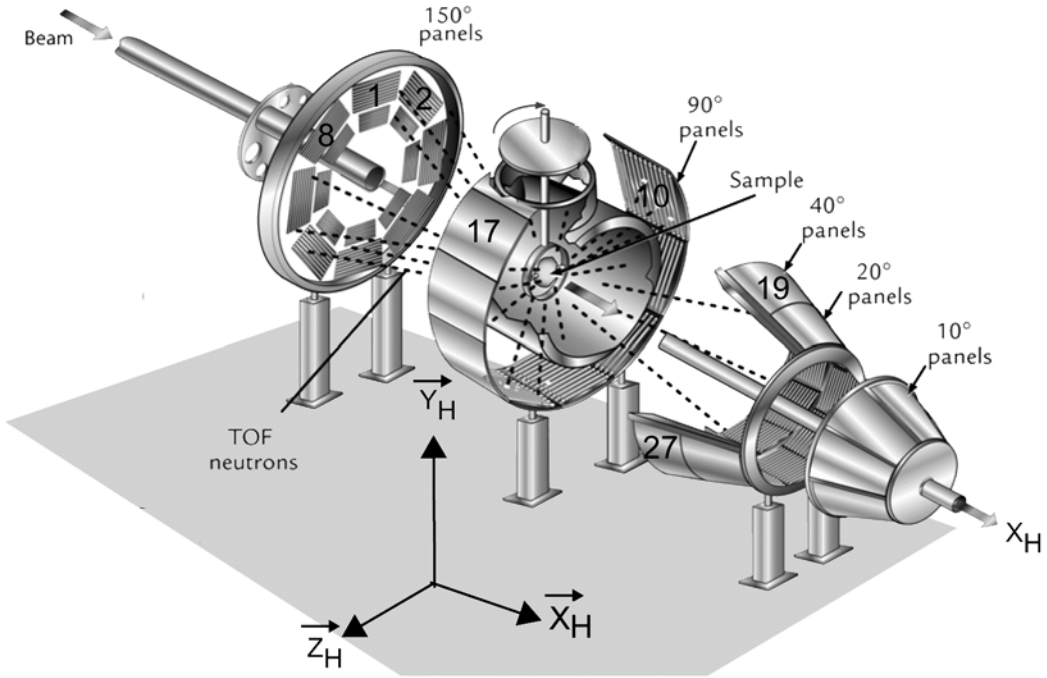

Figure 2. Diffraction spectra for aluminum recorded by one detector on each bank for four rotations. The sets of histograms correspond to 40, 90 and 140º diffraction angle (top to bottom). Relative intensity variations illustrate presence of texture. Resolution (peak widths) increases with increasing diffraction angle.

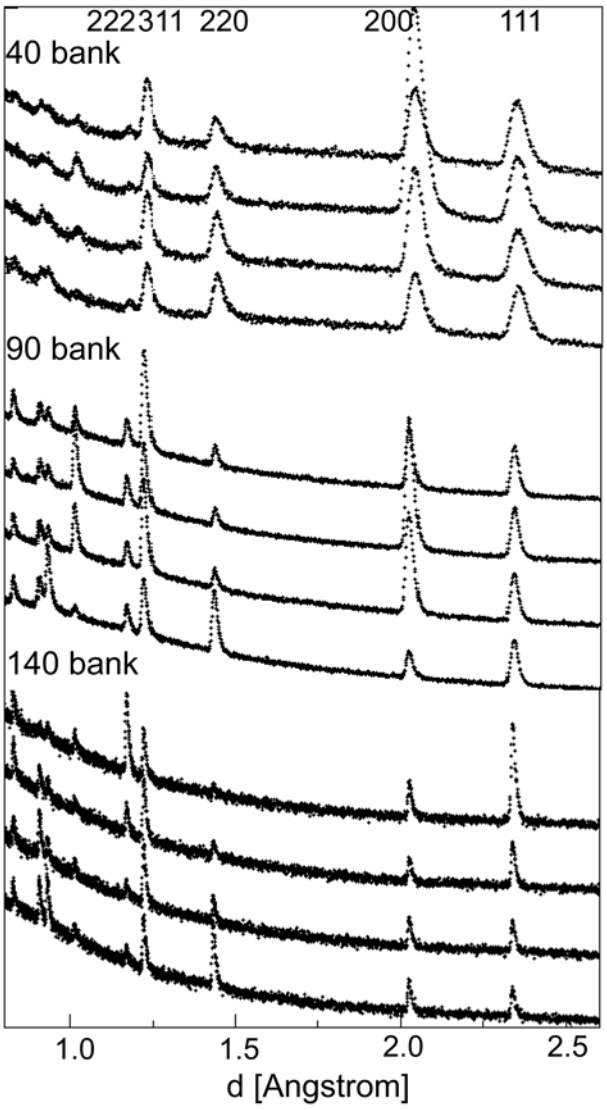

Figure 3. The HIPPO detector panels as they would appear on the pole figure sphere for the zero position of the sample on an equal area projection. Panel numbers correspond to the numbers in Table 2. The gap in the 90º detectors (panels 9 to 18) is due to the sample chamber opening. The beam direction is parallel to X_A. The panels roughly cover one quarter of the pole sphere for a single sample orientation.

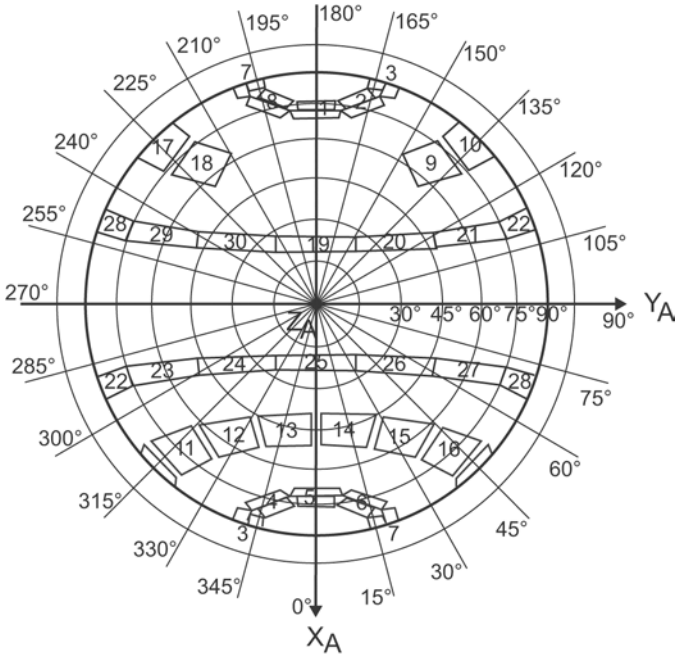

Figure 4. (a) The real form of the HIPPO detector panels. (b) The HIPPO detector panels modeled with 5^o pixels for GULUWIMV with additional interpolation of pole figure values across 5^o gaps. This modeling captures the shape of the panels better than treating each panel as a point-like detector. (Equal angular projection) (c) Pole figure coverage by detector panels for ECAP aluminum with four sample rotations (0^o, 45^o, 67.5^o, 90^o).

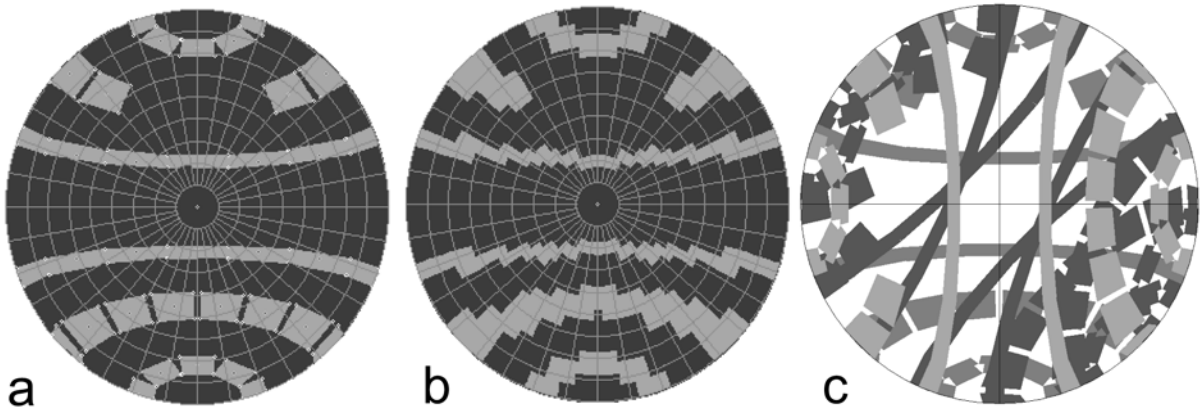

Figure 5. Stack of all diffraction spectra used in the refinement. All spectra are plotted at the same scale, dark shades indicate high intensities. (a) 140º bank, (b) 90º bank, (c) 40º bank.

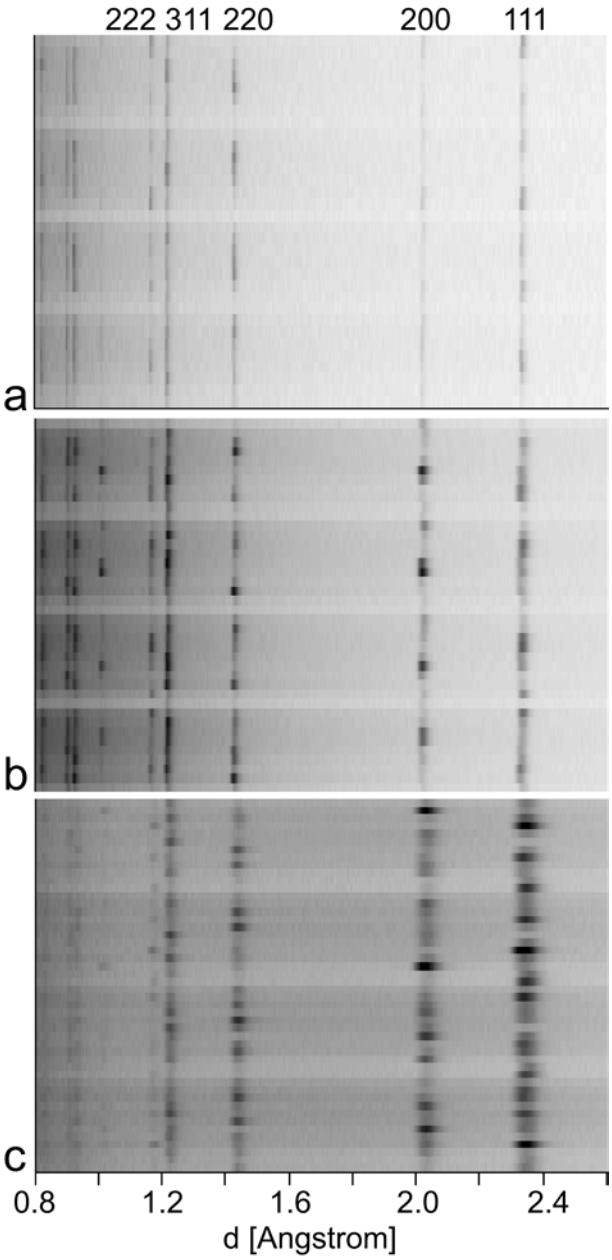

Figure 6. GULUWIMV ODF. Steps to generate an ODF with GULUWIMV for ECAP aluminum. Displayed are gamma sections in the vicinity of the main texture component. (a) Result after first WIMV iteration. (b) After ghost correction step to account for phon of 0.07. (c) After application of 7.5^{o} smoothing and 10^{o} filter to decrease noise. (d) The ODF can be used to generate spherical harmonic C_{lmn} coefficients. This is the reduced ODF, using only even l up to L = 12. Note that the gray areas in (d) correspond to negative orientation frequencies. Logarithmic scale. See Table 4 for numerical information

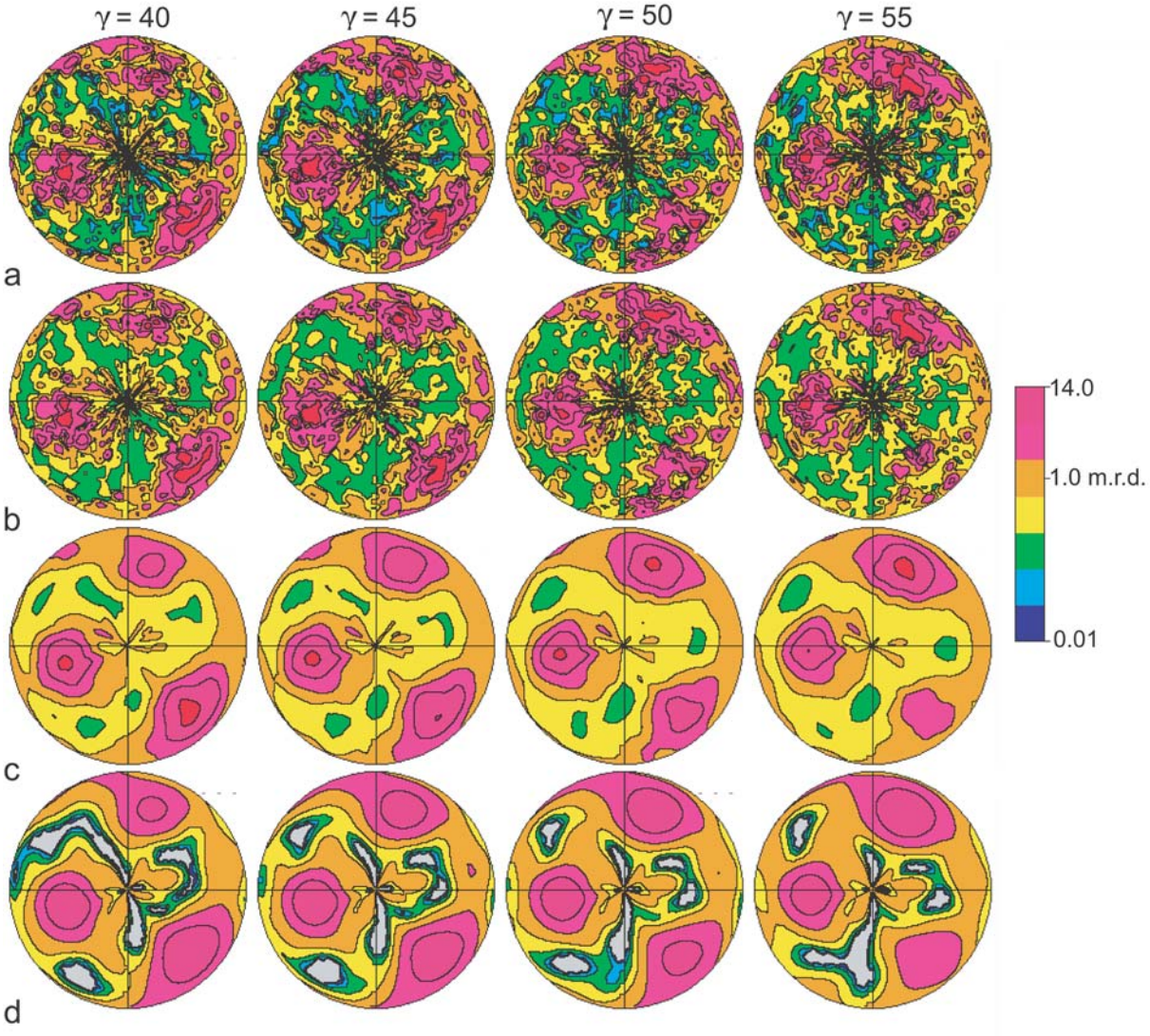

Figure 7. Comparison of ODFs for ECAP aluminum. Gamma sections in the vicinity of the main texture component. (a) GULUWIMV ODF with remaining ghost correction, 7.5° smoothing and 10° filter. (b) MAUD E-WIMV with 7.5° smoothing and 10° filter. (c) MAUD harmonic method L = 12 (only even l). (d) GSAS L = 12 (l even). Logarithmic scale. Gray areas correspond to negative ODF values. See Table 4 for additional numerical information.

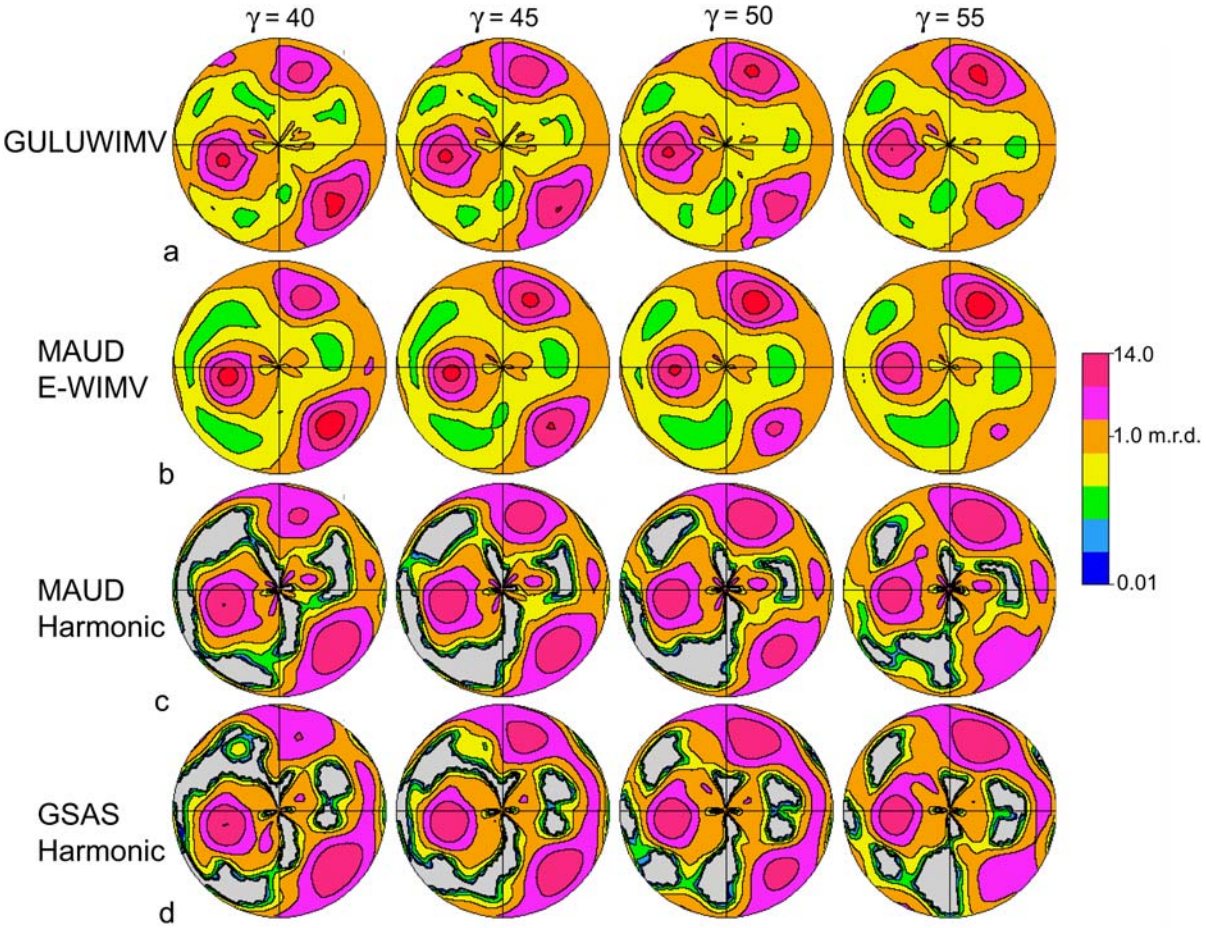

Figure 8. Comparison of pole figures for ECAP aluminum. (a) Recalculated pole figures from GULUWIMV ODF, filtered and smoothed. (b) Recalculated pole figures from MAUD E-WIMV filtered and smoothed. (c) Pole figures calculated from C_{lmn} coefficients output from the MAUD harmonic method variant (L = 12). (d) Pole figures from ODF generated with GSAS coefficients as described in the text (L = 12). Logarithmic scale. Pole figures are oriented in the zero position of the sample (defined in Section 3, Figure 3). See Table 5 for numerical data.

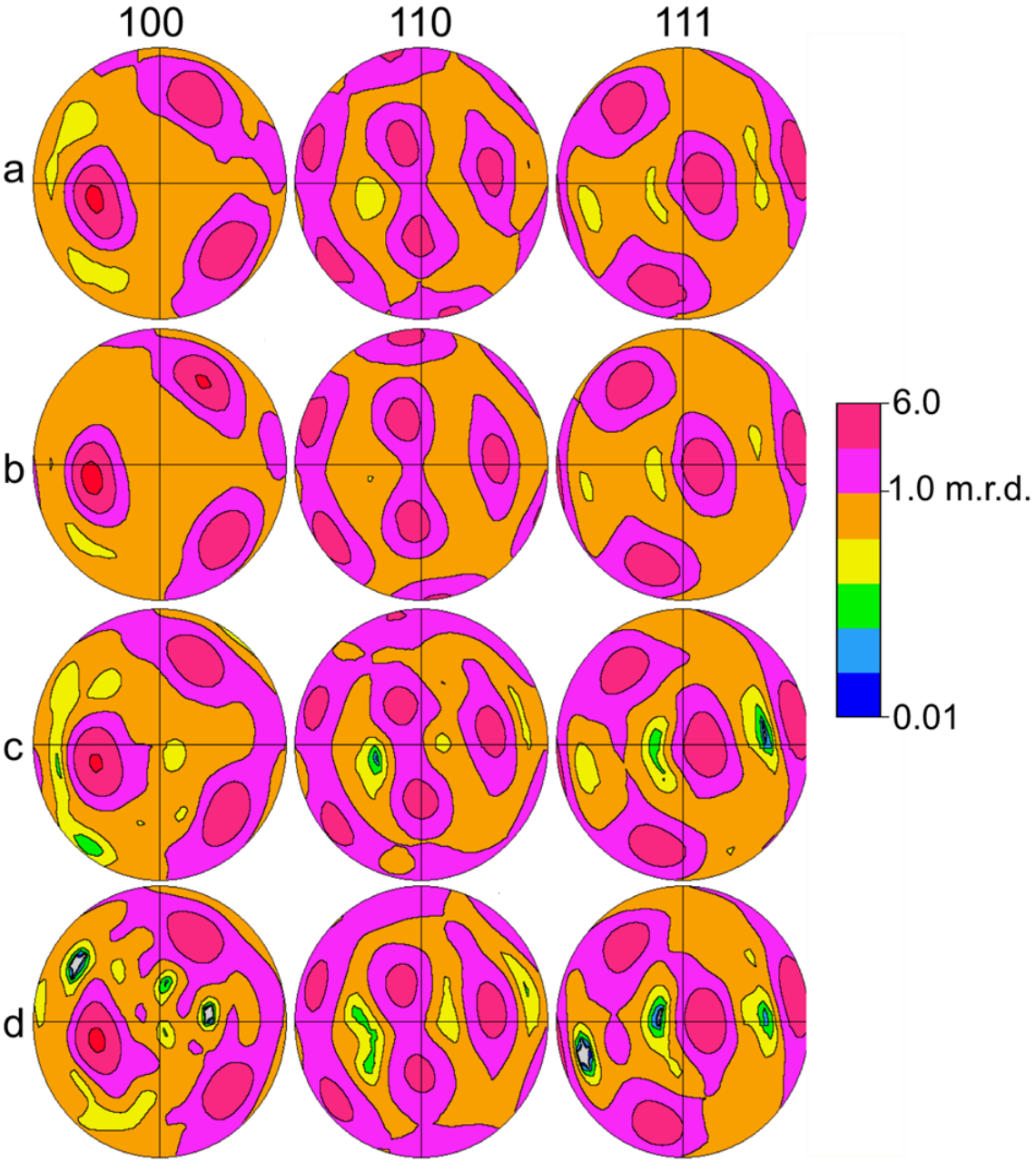

Figure 9. Comparison of the region below 1 m.r.d for the 100 pole figures of aluminum. (a) GULUWIMV, (b) MAUD E-WIMV (c-e) GSAS L= 12,14, and 16. Linear scale. Red regions are above 1 m.r.d.

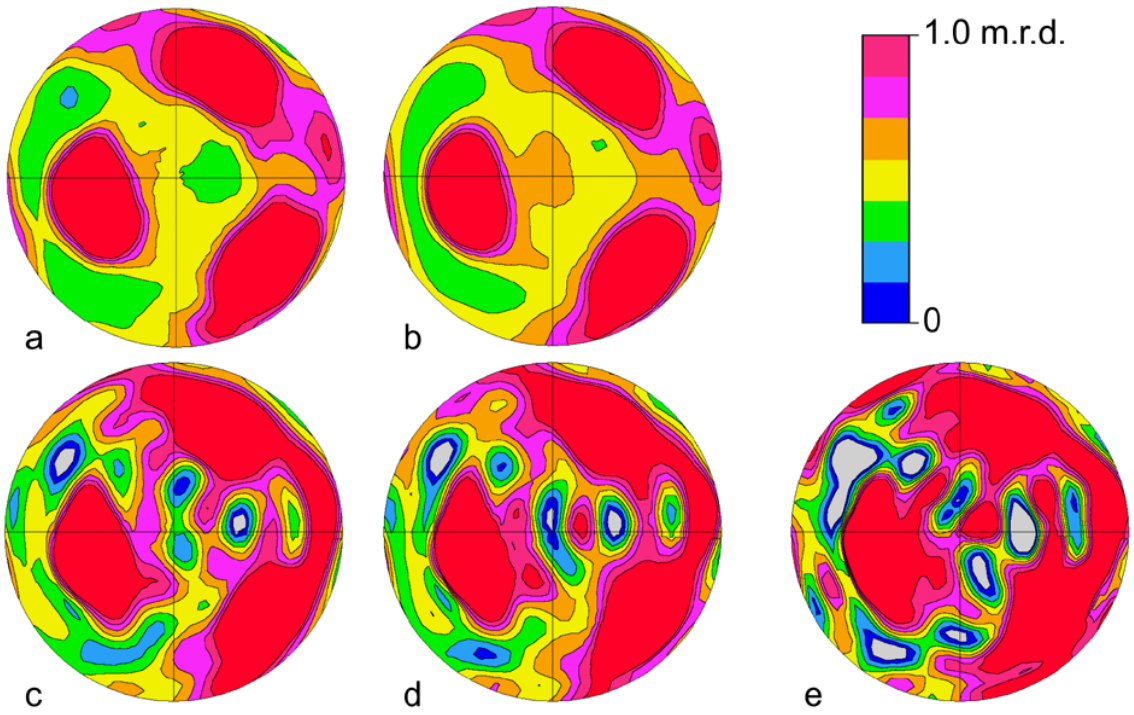

Figure 10. ECAP aluminum in the plain strain geometry of the experiment, with the transverse direction in the center and the shear plane oriented NE-SW. (SPN shear plane normal, SD shear direction) Top: rotated pole figures measured with HIPPO (MAUD E-WIMV method). Bottom: pole figures measured on the Berkeley EBSD system. Linear contour scale.